

Physics-Embedded Neural ODEs for Learning Antagonistic Pneumatic Artificial Muscle Dynamics

Xinyao Wang and Jonathan Realmuto

Abstract—Pneumatic artificial muscles (PAMs) enable compliant actuation for soft wearable, assistive, and interactive robots. When arranged antagonistically, PAMs can provide variable impedance through co-contraction but exhibit coupled, nonlinear, and hysteretic dynamics that challenge modeling and control. This paper presents a hybrid neural ordinary differential equation (Neural ODE) framework that embeds physical structure into a learned model of antagonistic PAM dynamics. The formulation combines parametric joint mechanics and pneumatic state dynamics with a neural network force component that captures antagonistic coupling and rate-dependent hysteresis. The forward model predicts joint motion and chamber pressures with a mean R^2 of 0.88 across 225 co-contraction conditions. An inverse formulation, derived from the learned dynamics, computes pressure commands offline for desired motion and stiffness profiles, tracked in closed loop during execution. Experimental validation demonstrates reliable stiffness control across 126-176 N/mm and consistent impedance behavior across operating velocities, in contrast to a static model, which shows degraded stiffness consistency at higher velocities.

Index Terms—Pneumatic artificial muscles, Soft robotics, Antagonistic actuation, Neural ordinary differential equations, Physics-informed learning

I. INTRODUCTION

Soft pneumatic actuators are widely used in wearable and assistive robots due to their inherent compliance, lightweight construction, and ability to generate human-compatible forces [1]–[4]. These properties enable safe physical interaction in rehabilitation, mobility assistance, and human augmentation applications. However, soft pneumatic actuators are nonlinear, hysteretic, and strongly pressure-dependent; their behavior varies with actuator design and operating conditions [5]–[8]. Accurately capturing these dynamics remains a fundamental challenge for model-based control.

Among soft pneumatic actuators, the McKibben-type pneumatic artificial muscles (PAMs) are widely studied due to their contractile behavior, high force-to-weight ratio, and well-characterized braid-bladder geometry [9], [10]. In robotic applications, PAMs are often arranged antagonistically to enable variable joint stiffness through co-contraction, analogous to human musculoskeletal control [11], [12]. This capability supports direct impedance modulation by antagonist co-activation [13], [14], rather than rendering impedance purely through high-bandwidth feedback [15]. However, the interaction between opposing muscles through a shared joint transmission

introduces coupled pressure, force, and motion dynamics that further complicates model-based control of PAM joints.

Classical analytical models of PAMs, such as the geometric formulation of Chou and Hannaford [10], capture quasi-static force-length-pressure relationships, but full rate-dependent dynamic effects are not modeled. Empirical extensions can improve accuracy in specific operating conditions [16], [17], but typically introduce additional parameters and may require retuning across operating regimes. For antagonistic configurations, prior work ranges from phenomenological quasi-static hysteresis/creep models for antagonistic joints (e.g., Maxwell-slip) [18] to analytic but relatively low-order dynamic joint models [19]. Learning-based methods, including neural networks and hybrid physics-informed models [20]–[26], offer greater flexibility but are often formulated in discrete time and frequently validated on single actuators. For stiffness-based impedance planning, however, the forward model must provide well-defined state sensitivities so that stiffness can be computed from force-state derivatives and embedded consistently in an inverse planning step.

On the control side, model predictive [27] and sliding mode [28] approaches have been applied to antagonistic PAM tracking, and decoupling strategies enable simultaneous position and stiffness control without explicit system identification [29]. For stiffness estimation, unscented Kalman filters provide sensorless angle and torque estimation in antagonistic PAM joints [30], [31]. Recent physics-informed learning approaches employ hybrid formulations to capture antagonistic coupling behavior [24]. However, none of these methods combine continuous-time learned dynamics with embedded physical structure in a framework that supports both forward prediction and inverse stiffness synthesis.

To meet this need, we adopt a hybrid continuous-time modeling approach based on neural ordinary differential equations (Neural ODEs) [32], which learn a continuous-time vector field with explicit states while allowing embedded physical submodels. We develop a hybrid Neural ODE for an antagonistic PAM joint that couples parametric joint mechanics and pressure dynamics with a learned nonlinear force term. The physics-based components capture inertial dynamics and pressure evolution, while the neural term captures unmodeled antagonistic interactions and rate-dependent hysteresis without introducing an explicit high-order hysteresis model.

Our objective is a continuous-time dynamic model of an antagonistic PAM joint with sufficient physical fidelity to support stiffness-aware feedforward planning. Given a desired joint trajectory $x_d(t)$ and time-varying stiffness profile $K_d(t)$, antagonistic muscle air masses ($m_f(t), m_e(t)$) are synthesized

This work was supported by NSF under award CMMI-2221315. The authors are with the Dept. of Mechanical Engineering, University of California, Riverside, CA, USA. Corresponding author J.R., jrealmuto@ucr.edu. Code available at: <https://github.com/jonreal/pneu-sim/tree/tmech-2026-submission>.

offline from the learned dynamics to reproduce the target motion and stiffness. The main contributions of this work are: (1) a hybrid Neural ODE model that embeds joint and pressure dynamics within a learned antagonistic PAM framework; (2) a velocity-dependent neural force term that captures hysteresis implicitly; and (3) a feedforward input synthesis procedure derived from the learned dynamics for offline motion and stiffness planning, validated experimentally on a physical antagonistic PAM joint.

II. HYBRID NEURAL ODE MODEL

This section develops a hybrid Neural ODE model for the antagonistic PAM joint (Fig. 1). The model describes passive dynamics under closed-valve conditions, where each chamber is sealed, and the air mass remains constant. Valve actuation and mass flow dynamics are outside the scope of the model. This separation is intentional so that the learned force model captures antagonistic coupling, rate-dependent hysteresis, and stiffness variation, as intrinsic properties of the mechanical state and chamber loading, independent of how that loading is established or regulated.

A. System States and Inputs

The antagonistic pneumatic artificial muscle (PAM) joint is modeled using a single generalized joint displacement coordinate (Fig. 1a). Joint rotation q is mapped to linear tendon displacement through the pulley radius r_p as

$$x = r_p q.$$

All subsequent dynamics are formulated in the linear displacement coordinate x rather than the joint angle q because the PAM forces act directly in the tendon space, making x a more natural representation for pressure and force modeling (Fig. 1a,b). The system state vector is defined as

$$\mathbf{x}(t) = [x(t) \quad \dot{x}(t) \quad P_f(t) \quad P_e(t)]^\top,$$

where x and \dot{x} denote joint displacement and velocity, and P_f and P_e are the absolute chamber pressures of the flexor and extensor PAMs, respectively. Including pressure states enables explicit representation of pneumatic dynamics and antagonistic co-contraction effects.

During closed-valve interaction, when each PAM chamber is sealed, the internal masses are constant; therefore, we treat the antagonistic chamber mass pair as an exogenous input to the model:

$$\mathbf{u}(t) = [m_f(t) \quad m_e(t)]^\top.$$

B. Joint Dynamics

The antagonistic joint is modeled as a single-degree-of-freedom translational system at the pulley interface (Fig. 1c). The joint dynamics are expressed as

$$m\ddot{x} = F_e + F_{\text{net}}, \quad (1)$$

where m is the effective mass reflected through the pulley, F_e represents externally applied forces, and F_{net} is the net interaction force generated by the antagonistic PAM pair.

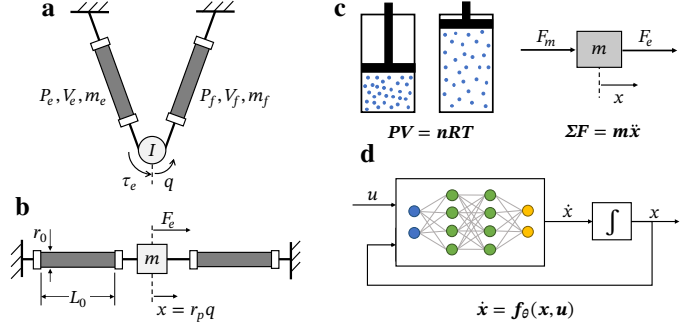


Fig. 1: System schematic and hybrid Neural ODE modeling components. **a** Antagonistic PAM joint with flexor (f) and extensor (e) muscles coupled through a pulley. **b** Equivalent translational model with chamber state variables and geometric parameters. **c** Embedded physics submodels: isothermal ideal gas law for pressure dynamics and Newton's second law for joint mechanics. **d** Neural ODE architecture with a learned vector field $f_\theta(\mathbf{x}, \mathbf{u})$, integrated forward in time to predict state trajectories.

Rather than decomposing F_{net} into separate analytical PAM force models, it is represented as a learned nonlinear function. This formulation allows the model to capture unmodeled effects such as rate-dependent hysteresis and antagonistic coupling without relying on explicit force-length-pressure mappings or actuator-specific stiffness parameters.

C. PAM Pressure Dynamics

When a PAM chamber is sealed, the chamber air mass is (approximately) invariant, $\dot{m}_i = 0$, for actuator $i \in \{f, e\}$ (Fig. 1c). Pressure, however, is not invariant since it varies with chamber volume as the joint moves. Under an isothermal ideal-gas approximation,

$$P_i(t) = C \frac{m_i}{V_i(x(t))}, \quad (2)$$

where $C = RT/m_{\text{air}}$ lumps the ideal-gas coefficient (universal gas constant R , absolute temperature T , and air molar mass m_{air}). So the same chamber mass m_i produces different pressures at different configurations through the volume map $V_i(x)$. This distinction motivates parameterizing the interaction force by the chamber masses rather than instantaneous pressures.

The chamber pressure dynamics are derived from taking the time derivative of the ideal gas law under an isothermal assumption in (2). For actuator $i \in \{f, e\}$, the pressure rate is written as

$$\dot{P}_i = C \left(\frac{\dot{m}_i}{V_i(x)} - \frac{m_i \dot{V}_i(x, \dot{x})}{V_i(x)^2} \right), \quad (3)$$

where P_i is the absolute chamber pressure, m_i is the internal air mass, \dot{m}_i is the mass flow rate into the chamber, and $V_i(x)$ is the chamber volume. In practice, temperature variation, leakage, and unmodeled pneumatic effects are not explicitly measured; therefore, C is treated as a learnable parameter during identification.

D. Volume-Displacement Relationship

McKibben-type PAMs consist of an elastomeric bladder enclosed by a braided sleeve with inextensible fibers. This geometry couples axial length and radial expansion: as internal pressure increases, the muscle shortens and bulges outward, with the braid angle adjusting to satisfy the fiber-length constraint. The chamber volume is therefore a function of muscle length alone.

Modeling each PAM as a cylinder with a displacement-dependent radius, the chamber volumes are

$$\begin{aligned} V_f(x) &= \pi r_f(x)^2 (L_0 - x), \\ V_e(x) &= \pi r_e(x)^2 (L_0 + x), \end{aligned} \quad (4)$$

where L_0 is the nominal (rest) muscle length, and $r_f(x)$ and $r_e(x)$ denote the effective radii of the flexor and extensor PAMs.

The radius-length coupling follows from the inextensible braid constraint. Assuming a linear coupling about the nominal configuration gives

$$\begin{aligned} r_f(x) &= r_0 + \nu \frac{r_0}{L_0} x, \\ r_e(x) &= r_0 - \nu \frac{r_0}{L_0} x, \end{aligned}$$

where r_0 is the nominal PAM radius and ν is a deformation coefficient determined by braid geometry. Differentiating (4) gives the time derivatives of volume:

$$\begin{aligned} \dot{V}_f(x, \dot{x}) &= \pi \dot{x} \left[2r_f(x)(L_0 - x)\nu \frac{r_0}{L_0} - r_f(x)^2 \right], \\ \dot{V}_e(x, \dot{x}) &= -\pi \dot{x} \left[2r_e(x)(L_0 + x)\nu \frac{r_0}{L_0} - r_e(x)^2 \right]. \end{aligned}$$

E. Forward Hybrid Neural ODE Model

The antagonistic PAM dynamics are constructed by combining the parametric joint mechanics in (1) and pressure dynamics in (3) with a learnable nonlinear force f_θ , parameterized by θ (Fig. 1d). This yields a hybrid neural ordinary differential equation that preserves physical structure while enabling the model to represent nonlinear and rate-dependent effects from data. The system evolves according to:

$$\dot{\mathbf{x}} = \begin{bmatrix} \dot{x} \\ \ddot{x} \\ \dot{P}_f \\ \dot{P}_e \end{bmatrix} = \begin{bmatrix} \dot{x} \\ \frac{1}{m}(F_e + f_\theta(x, \dot{x}, m_f, m_e)) \\ C \left(\frac{\dot{m}_f}{V_f(x)} - \frac{m_f \dot{V}_f(x, \dot{x})}{V_f(x)^2} \right) \\ C \left(\frac{\dot{m}_e}{V_e(x)} - \frac{m_e \dot{V}_e(x, \dot{x})}{V_e(x)^2} \right) \end{bmatrix}, \quad (5)$$

where $f_\theta(x, \dot{x}, m_f, m_e)$ represents the learnable interaction force from the antagonistic PAM pair.

For compactness, (5) is written as

$$\dot{\mathbf{x}} = \mathbf{f}_\Theta(\mathbf{x}, \mathbf{u}, F_e), \quad (6)$$

where the learnable parameter set is

$$\Theta = \{m, C, \nu, \theta\},$$

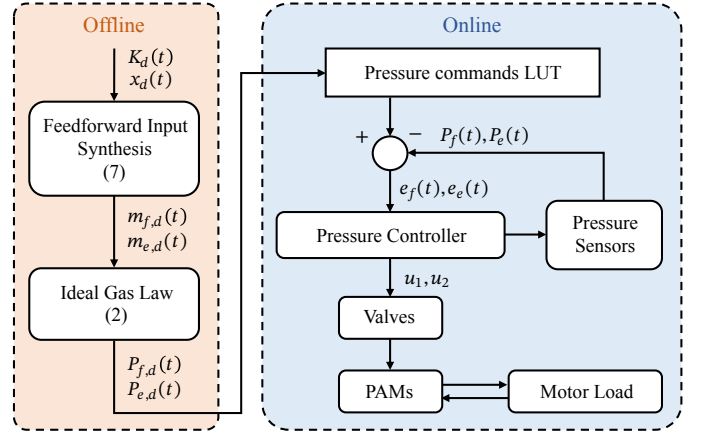


Fig. 2: Offline-to-online validation workflow. Desired motion $x_d(t)$ and stiffness $K_d(t)$ profiles are processed through the inverse formulation to produce air mass trajectories, converted to pressure commands via the ideal gas law, and stored in a lookup table. During online execution, the pressure controller tracks the precomputed commands using discrete valve pulsing to drive the antagonistic PAM joint.

consisting of the reflected mass m , gas coefficient C , geometric deformation coefficient ν , and neural network weights θ . This formulation preserves the analytical structure of joint and pneumatic dynamics while allowing the learned component to capture nonlinear and rate-dependent effects. The continuous-time representation avoids discretization bias and enables training from experimental data sampled at arbitrary rates.

F. Feedforward Input Synthesis via Constrained Optimization

To validate the learned dynamics, an inverse formulation is used to synthesize pressure commands for prescribed motion and stiffness profiles. During execution, the pressure controller tracks the precomputed commands to drive the antagonistic joint (Fig. 2). Given a desired joint trajectory $x_d(t)$ with corresponding velocity $\dot{x}_d(t)$, acceleration $\ddot{x}_d(t)$, and a target stiffness profile $K_d(t)$, we synthesize a feedforward antagonistic input at each time step by solving a constrained optimization problem for the chamber air masses (m_f, m_e). The optimization is evaluated at the desired operating point ($x_d(t), \dot{x}_d(t)$) and enforces dynamic consistency with $\ddot{x}_d(t)$.

The stiffness $K(t)$ is defined as a *translational stiffness* at the pulley interface (N/mm),

$$K = \frac{\partial f_\theta}{\partial x}.$$

Because the learned force model $f_\theta(\cdot)$ uses piecewise-linear activations (LeakyReLU), the derivative $\partial f_\theta / \partial x$ is piecewise constant and discontinuous at activation boundaries. To obtain a smooth stiffness estimate at a given operating point, we approximate the local slope using a second-order central finite-difference:

$$\begin{aligned} \hat{K}(x, \dot{x}, m_f, m_e) &= (f_\theta(x + 2h, \dot{x}, m_f, m_e) \\ &+ f_\theta(x + h, \dot{x}, m_f, m_e) \\ &- f_\theta(x - h, \dot{x}, m_f, m_e) \\ &- f_\theta(x - 2h, \dot{x}, m_f, m_e)) / (6h) \end{aligned}$$

where h is a small displacement increment used to approximate the local slope of the force-displacement relationship at the operating point. This scheme averages central difference estimates at step sizes h and $2h$, which improves robustness to local irregularities in $f_\theta(\cdot)$ while retaining second-order accuracy.

At each time sample t_k , given the desired trajectory point $(x_{d,k}, \dot{x}_{d,k}, \ddot{x}_{d,k})$ and target stiffness $K_{d,k}$, we solve for the chamber masses (m_f, m_e) via

$$\begin{aligned} \min_{m_f, m_e} \quad & (\hat{K}(x_{d,k}, \dot{x}_{d,k}, m_f, m_e) - K_{d,k})^2 \\ \text{s.t.} \quad & |m\ddot{x}_{d,k} - f_\theta(x_{d,k}, \dot{x}_{d,k}, m_f, m_e)| \leq \varepsilon, \end{aligned} \quad (7)$$

where the constraint enforces dynamic consistency with the desired acceleration. The tolerance $\varepsilon = 0.001$ mN is not always satisfied exactly; rather, it serves as a tight target that drives the solution toward the desired acceleration and improves tracking performance compared with looser tolerances.

This procedure yields an optimal antagonistic mass pair, $\mathbf{u}^*(t) = [m_f^*(t) \ m_e^*(t)]^\top$, that is dynamically consistent with the desired motion while matching the target local stiffness at the operating point. The key intuition is that, under sealed interaction, air mass is the invariant chamber quantity: joint motion changes pressure through volume change, whereas the mass parameterizes the antagonistic loading state that determines the force-displacement slope.

III. MODEL IDENTIFICATION AND TRAINING

This section describes the learning objective and training procedure used to identify the parameters of the hybrid Neural ODE introduced in (5) in Section II-E. Physical parameters and neural network weights are learned jointly from experimental trajectories by minimizing a trajectory-level prediction error.

A. Training Objective

The predicted state trajectory $\hat{\mathbf{x}}(t) = [\hat{x}, \hat{\dot{x}}, \hat{P}_f, \hat{P}_e]^\top$ is obtained by integrating the hybrid Neural ODE (6) forward in time:

$$\dot{\hat{\mathbf{x}}} = \mathbf{f}_\Theta(\hat{\mathbf{x}}, \mathbf{u}, F_e), \quad \hat{\mathbf{x}}(0) = \mathbf{x}_0,$$

where \mathbf{x}_0 is the measured initial state, $\mathbf{u} = [m_f, m_e]^\top$ are the chamber masses (constant under closed-valve conditions), and $F_e(t)$ is the applied external force.

The parameters Θ of the hybrid Neural ODE are identified by minimizing a trajectory-level mean squared error between predicted and measured joint motion and chamber pressures. The loss function is defined as:

$$\begin{aligned} \mathcal{L} = 100 \cdot \frac{1}{N} \sum_{k=1}^N & \left[(\hat{x}_k - x_k)^2 + (\hat{\dot{x}}_k - \dot{x}_k)^2 \right] \\ & + \frac{1}{N} \sum_{k=1}^N \left[(\hat{P}_{f,k} - P_{f,k})^2 + (\hat{P}_{e,k} - P_{e,k})^2 \right], \end{aligned}$$

where N denotes the number of time samples in the trajectory. The weighting coefficients are selected based on the numerical scale of the state variables, with joint displacement and velocity expressed in millimeters (mm) and millimeters per second (mm/s), and pressures expressed in kilopascals (kPa).

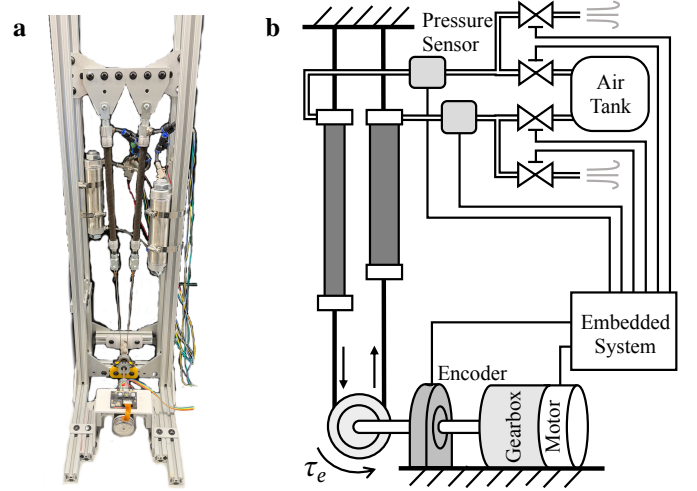


Fig. 3: Experimental antagonistic PAM platform. **a** Physical setup showing the antagonistic PAM pair, pulley joint, and DC motor. **b** System schematic: each PAM chamber is independently regulated through a pair of three-way solenoid valves supplied from a common air tank, with chamber pressures measured by inline pressure sensors. An embedded controller coordinates valve actuation, motor commands, and sensor acquisition.

B. Staged Learning Strategy

Direct optimization of the hybrid Neural ODE from random initialization was found to be unstable due to the absence of explicit dissipation in the joint dynamics. To address this issue, a staged learning strategy was adopted, consisting of the following steps:

- **Initialization with auxiliary damping:** Training is initialized by augmenting the joint dynamics with an auxiliary viscous damping term of the form $B\dot{x}$. This term is used only to stabilize early-stage numerical integration.
- **Progressive damping removal:** Over successive training stages, the auxiliary damping coefficient is gradually reduced from an initial value of 6500 kg/s to zero. Each stage is initialized from the previous one, and the final learned model contains no explicit damping term.
- **Progressive dataset expansion:** Training begins from symmetric ($m_f = m_e$), near-center operating conditions and progressively expands to more biased and asymmetric antagonistic operating points, followed by intermediate conditions, to improve coverage of the co-contraction space.

The physical parameters and neural network weights are optimized jointly during training.

C. Physical Parameter Initialization

Initial values for the physical parameters in the hybrid Neural ODE were obtained from actuator datasheets, geometric relations, and experimental characterization:

- **Equivalent mass m :** Computed from the reflected inertia of the motor and transmission through the pulley radius.

- **Geometric deformation coefficient ν** : Derived from the Poisson ratio definition and the geometric relations of a McKibben-type braided actuator [10]. Specifically,

$$\nu = \cot^2(\theta_{braid}),$$

where θ_{braid} is the fiber braid angle at the nominal configuration.

- **Gas coefficient C** : Initialized from nominal ideal gas values based on the universal gas constant R , room temperature T , and the molar mass of air m_{air} . As negligible deviation was observed during training, C is treated as a fixed constant in the final model.

The physical parameters were constrained to remain positive during optimization using a Softplus transformation.

D. Numerical Implementation

The hybrid Neural ODE is integrated using a fifth-order Tsitouras solver with adjoint sensitivity gradients. The force component $f_\theta(\cdot)$ uses two fully connected hidden layers with 96 neurons each and LeakyReLU activation functions.

Training was conducted for up to 5000 epochs using the Adam optimizer with an initial learning rate of 1×10^{-2} . The learning rate was reduced by a factor of 0.95 upon loss plateau, and early stopping was applied with a patience of 100 epochs. The model with the lowest training loss was retained.

IV. EXPERIMENTAL SETUP

This section describes the experimental platform and data collection procedures used for model identification and validation of the antagonistic PAM joint. Two experimental setups were employed: a single PAM characterization platform used to obtain static force profiles for air mass estimation, and an antagonistic joint platform used for dynamic system identification and validation.

A. Experimental Antagonistic Joint Platform

The antagonistic joint platform used for dynamic model identification and validation is shown in Fig. 3. Two identical PAMs (DMSP-10-200N, Festo) were mounted in an antagonistic configuration and routed symmetrically over a pulley to form a single-degree-of-freedom joint. Each PAM was connected to the joint shaft via a steel tendon secured to a 3D-printed fixture, ensuring axial loading and symmetric routing.

A brushless DC motor (200142, Maxon Group) with a gearbox (260552, Maxon Group) was coupled to the joint shaft to apply external torque excitation. Joint position was measured using an incremental magnetic encoder (AMT203-V, CUI Devices). Chamber pressures were measured independently for each PAM using Honeywell 150PG2A3 pressure sensors mounted near the muscle inlets. A small preload was applied manually to both PAMs to remove slack and ensure consistent tendon tension.

Table I summarizes the system parameters. Parameters marked with \dagger were used only to initialize the hybrid Neural ODE training and were not treated as fixed identified constants.

TABLE I: System parameters used in the model. Parameters marked with \dagger denote initialization values used for neural network training.

Symbol	Description	Value	Unit
r_0	Nominal PAM radius	5.00×10^{-3}	m
L_0	Nominal PAM length	0.2	m
r_p	Pulley radius	6.875×10^{-3}	m
I_{motor}	Motor rotor inertia	9.25×10^{-6}	kg·m ²
$I_{gearbox}$	Gearbox inertia	5.00×10^{-7}	kg·m ²
N	Gear ratio	36:1	-
I	Equivalent joint inertia	1.20×10^{-2}	kg·m ²
m^\dagger	Equivalent linear mass	2.53×10^2	kg
θ_{braid}	Braid angle	25	deg
ν^\dagger	Deformation coefficient	4.60	-
R	Gas constant	8.314	J/(mol·K)
T	Temperature	295.15	K
m_{air}	Air molar mass	2.897×10^{-2}	kg/mol
C^\dagger	Gas coefficient	8.47×10^4	m ² /s ²

B. Pressure Regulation and Embedded System

Compressed air was supplied from a main storage tank (N310415, PORTER-CABLE) and passed through an inline pneumatic reservoir (US14227-S0400, SMC) to reduce pressure fluctuations. The reservoir output was divided into two branches, each connected to a PAM through a pair of miniature three-way solenoid valves (SY113-SMO-PM3-F, SMC), enabling independent inflation and exhaust.

Pressure regulation was achieved using a discrete valve pulsing strategy. At each control cycle, the measured pressure was compared to the desired setpoint. If the error exceeded the fixed deadband, a short inflation or exhaust pulse was applied depending on the error sign. Inflation pulses lasted 10 ms, exhaust pulses 15 ms, and a 20 ms refractory period was enforced to allow pressure stabilization. These timing parameters were selected empirically to ensure reliable valve operation without overshoot or flow interruption and were not obtained through formal optimization. Once the target pressure was reached, both valves were closed, isolating the PAM as a sealed pneumatic volume.

A BeagleBone Black Wireless embedded controller coordinated valve actuation, motor torque commands, and synchronized data acquisition for both experimental setups. All sensor signals were sampled at 1 kHz and recorded for offline processing.

C. Training Excitation

The antagonistic joint was excited using sinusoidal motor torque inputs only. Three excitation frequencies were used during data collection: 0.5 Hz, 1 Hz, and 2 Hz. For each frequency, two torque amplitudes were applied by commanding motor currents of 1 A (0.918 N·m) and 1.5 A (1.377 N·m). These trials were repeated under multiple co-contraction conditions to generate a dataset covering a range of stiffness configurations for model training and held-out validation. Model generalization was evaluated using an independent validation experiment consisting of a perturbation signal with a 0.5 A amplitude. This perturbation validation dataset was not used during model training.

D. Air Mass Estimation

The chamber air masses (m_f, m_e) are not directly measurable but can be inferred from pressure and position measurements. Using offline single-PAM characterization, quasi-static loading and unloading force profiles were measured across a range of pressures and fitted with polynomial surfaces. These profiles relate force, displacement, and air mass for each hysteresis branch.

Because the gas coefficient, C , and the deformation coefficient, ν , are unknown before training, air masses cannot be computed directly from pressure. Instead, they are estimated at equilibrium configurations where the flexor and extensor forces balance. Because hysteresis causes the equilibrium position to differ with velocity direction, masses are estimated at both loading-to-unloading and unloading-to-loading zero-torque crossings, then averaged to reduce bias. After training, C and ν are identified, and air masses are computed directly via (2).

V. RESULTS

A. Forward Model Accuracy

The hybrid Neural ODE forward model was trained using 29 datasets selected from a total of 225 collected under distinct co-contraction conditions. Co-contraction conditions were defined on a grid of commanded pressure pairs ($P_{f,d}, P_{e,d}$) (Fig. 4a); the corresponding air masses used as model inputs were obtained via the mass estimation procedure (Section IV-D) (Fig. 4b). The datasets were chosen using a staged coverage strategy over the pressure grid. Training began from symmetric pairs (10-10 to 80-80 psi), followed by asymmetric conditions with increasing pressure differences (40-50 to 10-80 psi) in both directions, forming an ‘‘X-shaped’’ pattern. Additional datasets along lines with the same total pressure were included to widen coverage around intermediate co-contraction levels. This intentional, non-uniform selection maximizes coverage of symmetric and asymmetric regimes while limiting training size. The remaining datasets were reserved for evaluation.

For each pressure pair (or equivalently, mass pair), the model predicted the joint displacement x , velocity \dot{x} , and PAM pressures P_f and P_e . The coefficient of determination R^2 was computed between predicted and measured trajectories to quantify prediction accuracy. Across all responses and operating conditions, the mean R^2 value was 0.88. Figure 4 summarizes the R^2 values across all 225 operating conditions, with the training datasets highlighted with circles for reference. The model generalizes well across the operating grid, with reduced accuracy at extreme co-contraction conditions where one muscle approaches slack and the underlying dynamics deviate from the pressurized regime assumed by the model. The dataset used for the time-series example in Fig. 5 is indicated by a star in Fig. 4.

Representative time-series results for one training dataset are shown in Fig. 5. The predicted joint motion and chamber pressures closely follow the measured trajectories throughout the excitation cycle. To further examine hysteresis, the corresponding force versus displacement (x - F) and pressure versus

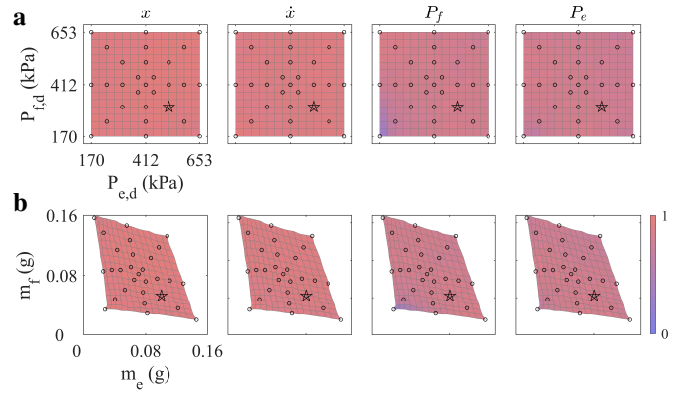


Fig. 4: Coefficient of determination (R^2) of the hybrid Neural ODE model over 225 operating conditions. Each grid intersection represents one dataset. The model achieves consistently high accuracy across the full co-contraction range, with an overall mean $R^2 = 0.88$. **a** R^2 in the desired pressure space ($P_{f,d}, P_{e,d}$). **b** R^2 in the corresponding air-mass space (m_f, m_e). Circles denote the operating condition used for training; other conditions were used to evaluate the forward model’s accuracy. The star marks the condition shown in Fig. 5.

force (P_f - F , P_e - F) loops are also shown for each frequency segment in Fig. 5.

A small phase lag is observed in the measured pressure signals, which is primarily introduced by the low-pass filtering implemented in the on-board signal conditioning during data acquisition (cutoff frequency 3 Hz). This filtering induces a frequency-dependent delay in the measured pressure signals. To enable fair visual comparison, the measured pressure signals were temporally aligned with the model predictions by estimating the dominant delay using cross-correlation. The estimated delays were approximately 31 ms, 40 ms, and 41 ms for excitation frequencies of 0.5, 1, and 2 Hz, respectively. This alignment is applied only for visualization purposes and does not affect model training or quantitative evaluation. The corresponding hysteresis loops under different excitation frequencies are also shown, enabling direct comparison between measured and predicted force-displacement and pressure-force relationships.

To further examine the learned interaction force, the net joint force $f_\theta(\cdot)$ was evaluated over joint displacement for representative antagonistic air-mass pairs spanning the operating range and for three velocities $\dot{x} \in \{-5, 0, 5\}$ mm/s. The resulting force-displacement curves are shown in Fig. 6. Near the neutral configuration, the force-position relationship is approximately linear, with increasing curvature at larger displacements and for asymmetric mass distributions. Changing the relative air masses shifts the equilibrium joint position, while increased co-contraction increases the local slope, corresponding to higher effective stiffness. Velocity-dependent offsets in the force curves indicate modest hysteresis effects consistent with the loading-unloading behavior of pneumatic artificial muscles.

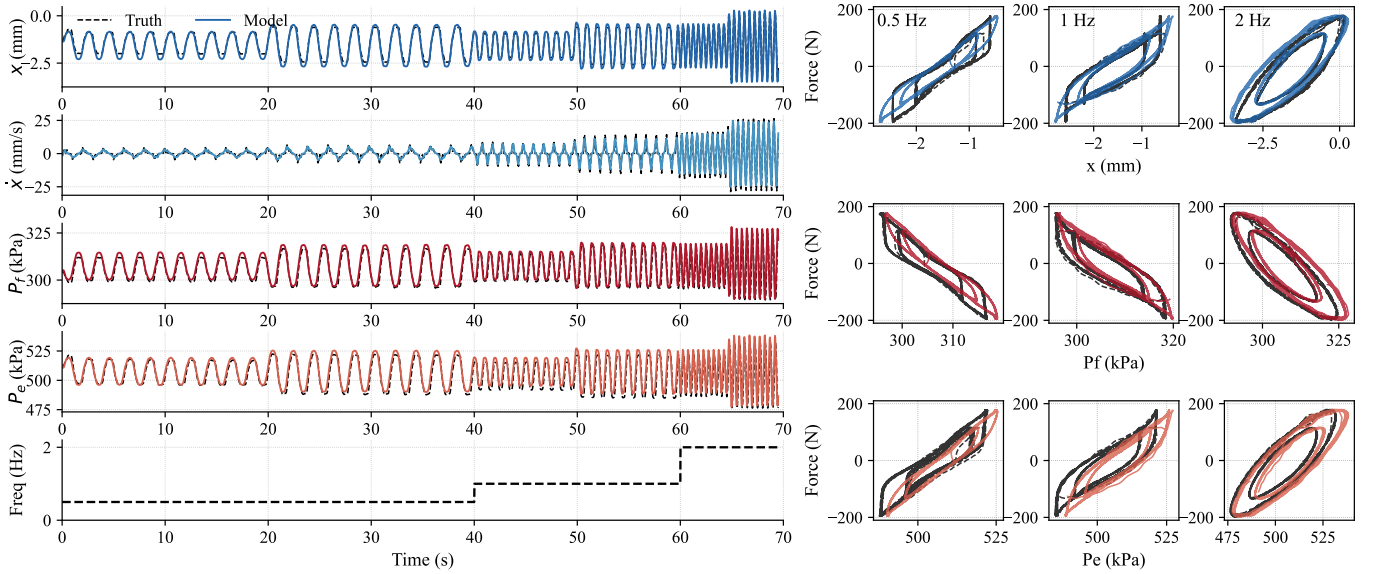


Fig. 5: Example comparison between the hybrid Neural ODE prediction and experimental measurements for one training dataset at $(P_{f,d}, P_{e,d}) = (206.8, 413.7)$ kPa (30, 60 psi). The model accurately reproduces the measured displacement x , velocity \dot{x} , and PAM pressures P_f and P_e . Right panels show measured (black dashed) and model-predicted (colored solid) hysteresis loops for force versus displacement (x - F), flexor pressure (P_f - F), and extensor pressure (P_e - F) at 0.5, 1, and 2 Hz.

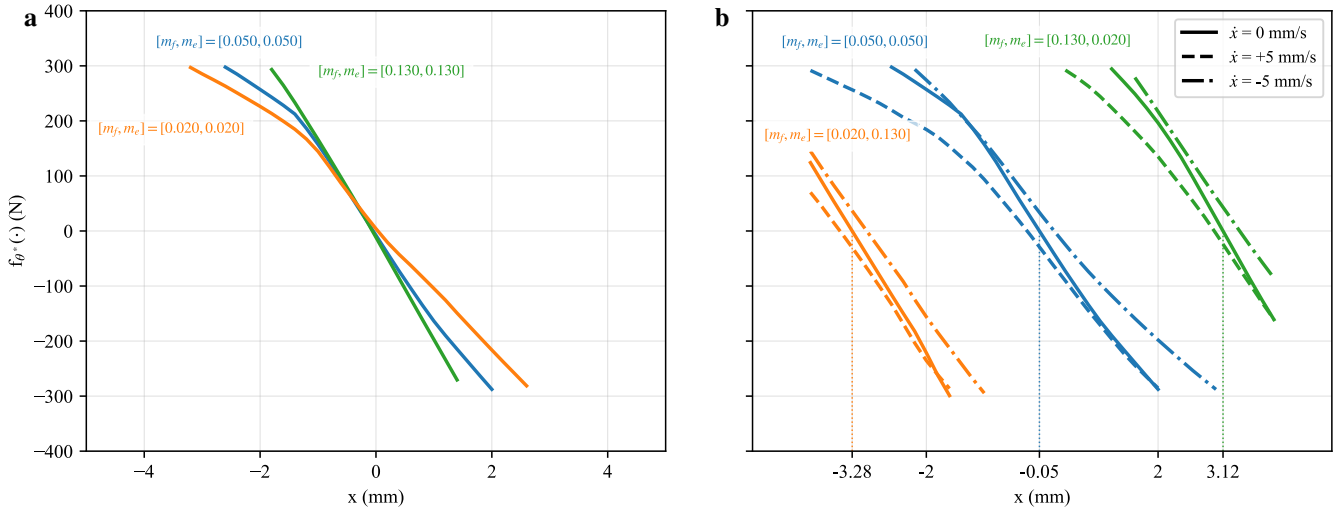


Fig. 6: Learned joint force $f_\theta(\cdot)$ as a function of joint displacement, evaluated at discrete flexor and extensor chamber masses (in grams) and velocities ($\dot{x} \in \{-5, 0, 5\}$ mm/s). **a** Force-displacement curves for symmetric mass conditions ($m_f = m_e$), showing stiffness variation with changing total air mass. **b** Force-displacement curves for representative asymmetric cases, including low-high (edge) and intermediate (mid) antagonist mass combinations. Dotted vertical lines indicate the equilibrium position (zero-force crossing) for each mass pair, showing how mass imbalance shifts the equilibrium.

B. Motion Synthesis Validation

1) *Amplitude variation:* At fixed frequency $f = 0.1$ Hz and desired stiffness $K_d = 150$ N/mm, sinusoidal trajectories with amplitudes $A \in \{0.5, 1.0, 1.5, 2.0\}$ mm were commanded. The resulting tracking errors are summarized in Fig. 7a. Error magnitude remains nearly constant across amplitudes, indicating that deviations are dominated by static friction effects near low-velocity motion reversals rather than by amplitude-dependent dynamics.

2) *Frequency variation:* With amplitude fixed at $A = 1.0$ mm and stiffness $K_d = 150$ N/mm, trajectories were commanded at $f \in \{0.1, 0.25, 0.5, 0.75, 1.0\}$ Hz. As shown in Fig. 7b, the mean tracking error increases slightly with frequency, reflecting limited representation of higher velocity motion in the training dataset. Inverse model validation was limited to 1 Hz because this range is representative of typical wearable robot motions. At higher frequencies, performance is mainly constrained by hardware limitations, as the discrete

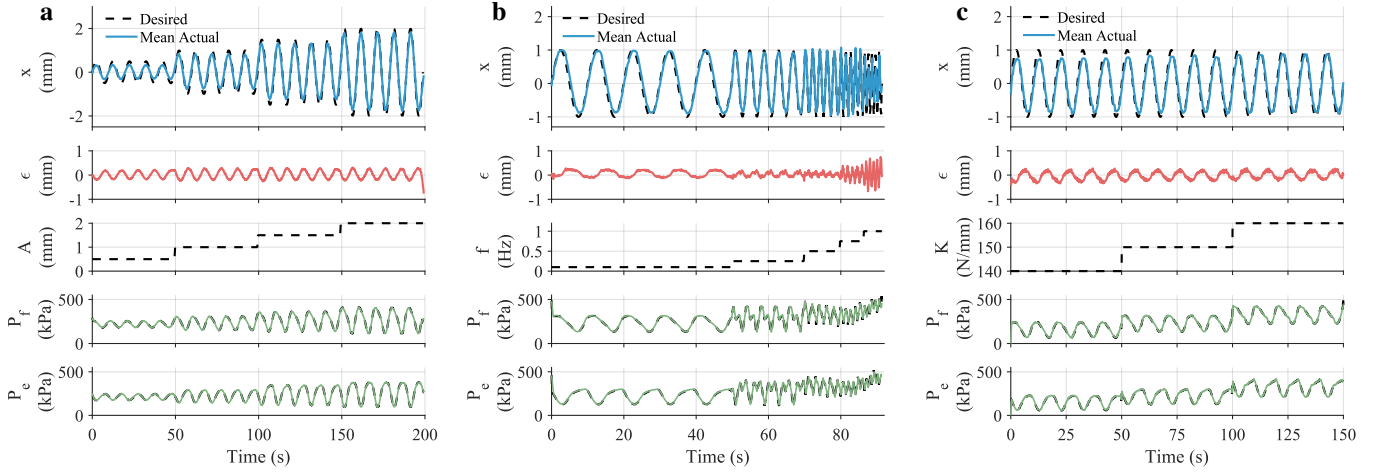


Fig. 7: Feedforward tracking validation under amplitude, frequency, and stiffness variation. **a** Tracking amplitude ($A = \{0.5, 1.0, 1.5, 2.0\}$ mm) under fixed frequency ($f = 0.1$ Hz) and stiffness ($K_d = 150$ N/mm). The nearly constant error magnitude suggests static friction dominates low velocity deviations. **b** Tracking performance across frequencies ($f = \{0.1, 0.25, 0.5, 0.75, 1.0\}$ Hz) with fixed amplitude ($A = 1.0$ mm) and stiffness ($K_d = 150$ N/mm). The tracking error increases slightly with frequency, consistent with limited training coverage at higher velocities. **c** Tracking performance under different stiffness levels ($K_d = \{140, 150, 160\}$ N/mm) at fixed amplitude ($A = 1.0$ mm) and frequency ($f = 0.1$ Hz). Comparable errors confirm consistent inverse model accuracy under varying co-contraction conditions.

valve-based pressure controller cannot accurately track commanded pressures.

3) *Stiffness variation*: To evaluate robustness with respect to stiffness modulation, stiffness was varied among $K_d \in \{140, 150, 160\}$ N/mm at fixed amplitude $A = 1.0$ mm and frequency $f = 0.1$ Hz. Tracking errors remain comparable across stiffness levels (Fig. 7c), indicating that stiffness modulation does not degrade motion tracking accuracy under the tested conditions.

C. Stiffness Synthesis Validation

To validate the model's stiffness predictions, the effective joint stiffness was identified experimentally using perturbation-based system identification under closed-valve conditions.

1) *System identification and stiffness estimation*: The effective stiffness K and damping B were identified using a linear spring-mass-damper model,

$$M(\ddot{x} - \ddot{x}_0) + B(\dot{x} - \dot{x}_0) + K(x - x_d) = F_e,$$

where the mass M was fixed to the effective mass, m , learned by the hybrid Neural ODE. The parameters K and B were identified by minimizing the sum of squared displacement errors between the measured response and the model integrated with `ode45`. A two-stage optimization was used: `patternsearch` for initial parameter search, followed by `fmincon` for local refinement. The external force F_e was derived from the commanded motor current and synchronized with the measured displacement.

2) *Perturbation protocol*: During perturbation for stiffness identification, the pressure controller is paused, and all valves are kept closed, ensuring constant chamber air masses throughout the identification window. A motor square torque pulse with a duration of 150 ms is applied to the joint immediately,

and the resulting joint response is used to identify K and B . This places the system in the closed-valve regime ($\dot{m}_i = 0$) that the learned model describes: if the servo remained active, valve pulses would alter the air masses and invalidate the model assumptions. Because the perturbation is applied without delay, identification is performed at the instantaneous operating condition along the ongoing trajectory.

A periodic trajectory with $A = 1.0$ mm and $f = 0.1$ Hz was tracked while the desired stiffness cycled through $K_d \in \{140, 150, 160\}$ N/mm. Each stiffness level was held for five cycles, and both positive and negative perturbation directions were applied for system identification.

Figure 8a illustrates the system response and stiffness validation. Perturbations are introduced at the peak, center, and trough of the tracking trajectory in both directions. The identified stiffness values follow the commanded stiffness schedule across the tested operating conditions.

To validate the stiffness range predicted by the trained model at the equilibrium position $x_0 = 0$ mm, desired stiffness values $K_d \in \{126, 136, 146, 156, 166, 176\}$ N/mm were commanded. For physical interpretation, this corresponds to an equivalent rotational stiffness range of $K_q \in [5.95, 8.31]$ N·m/rad. Positive and negative perturbations were applied, and stiffness was identified using the same procedure. As shown in Fig. 8b, the identified stiffness values span the predicted range. The lowest stiffness level exhibits a larger deviation from the target value, associated with operation near the lower co-contraction region, where one actuator loses effective tension and the system behavior departs from the pressurized dynamics represented in the model.

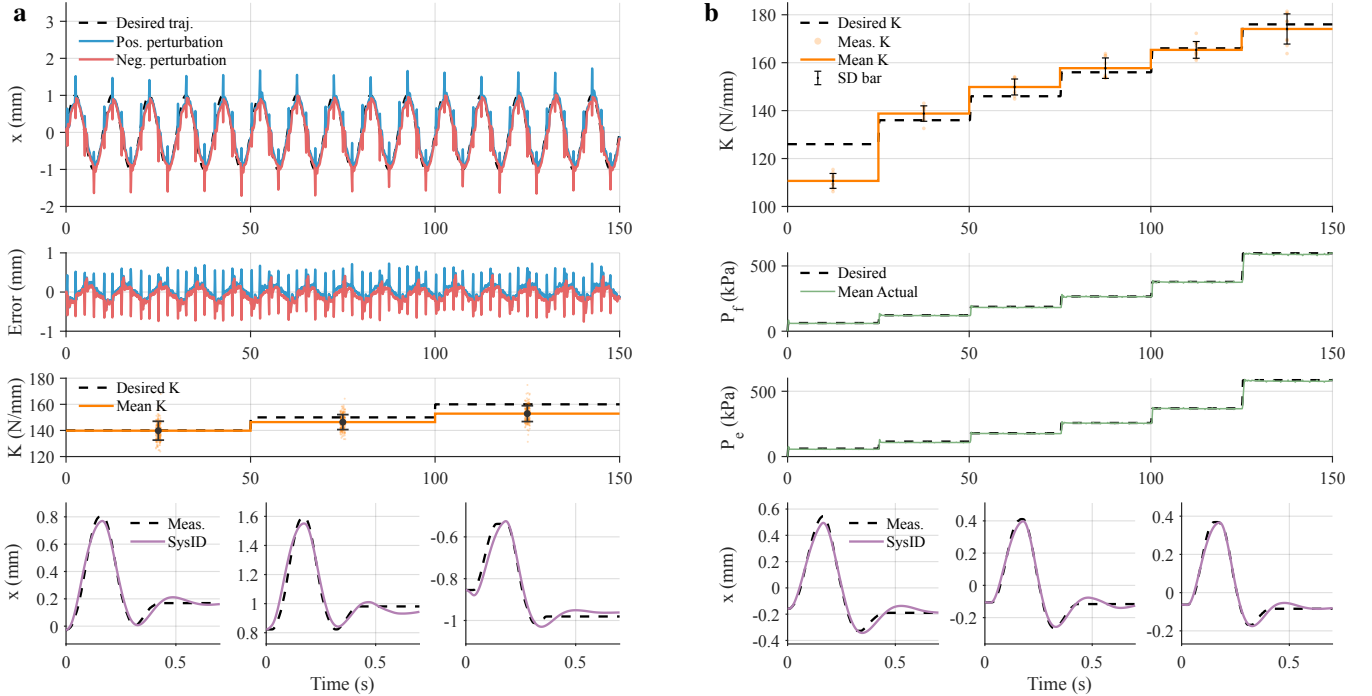


Fig. 8: Stiffness synthesis validation. **a** Time-varying stiffness tracking ($K_d \in \{140, 150, 160\}$ N/mm) during sinusoidal motion ($A = 1.0$ mm, $f = 0.1$ Hz). From top: joint displacement under positive (blue) and negative (red) perturbations; tracking error; identified stiffness (mean \pm SD from 300 perturbations) versus desired; representative perturbation responses and system identification fits at $x_0 \in \{0, +1, -1\}$ mm. **b** Stiffness range verification ($K_d \in \{126-176\}$ N/mm) at equilibrium ($x_0 = 0$ mm). From top: identified stiffness (60 perturbations); commanded and measured chamber pressures P_f , P_e ; representative perturbation responses at $K_d \in \{126, 146, 176\}$ N/mm.

D. Comparison with Equilibrium-Point Model

To assess whether velocity-dependent force modeling improves stiffness prediction, the hybrid Neural ODE was compared with an equilibrium-point (EP) model. The EP model captures the classical antagonistic intuition that differential pressure governs the equilibrium position, while total pressure governs stiffness [12], [13]. Assuming linear pressure-based mappings, the EP model can be described as

$$x_0 = \alpha_1(P_f - P_e) + \alpha_0, \quad K = \beta_1(P_f + P_e) + \beta_0,$$

which neglects hysteresis and rate-dependent effects. To ensure a fair comparison, the EP parameters were fit to the equilibrium and stiffness relationships extracted from the trained Neural ODE, so that both models operate from the same underlying data. Pressure commands were then computed using the same inverse procedure for both models.

Both models were evaluated under identical conditions using a sinusoidal trajectory with stepped stiffness targets. Perturbations were applied at zero and maximum velocity, and stiffness was identified using the same procedure described above. As shown in Table II and Fig. 9, the Neural ODE model maintains relatively consistent stiffness across velocities ($\Delta < 2.5\%$), whereas the EP model exhibits a substantially larger variation at maximum velocity ($\Delta = 8.2-11.6\%$, paired t -test, $p < 0.05$).

TABLE II: Identified joint stiffness for the Neural ODE (NN) and equilibrium point (EP) models.

Model	Part	Nominal (N/mm)		$\Delta(\%)$	p -value	
		$\dot{x} = 0$	$\dot{x} = \dot{x}_{\max}$			
NN	K_{low}	140	139.54	140.07	1.06	0.6036
	K_{mid}	150	146.96	145.83	2.26	0.1075
	K_{high}	160	152.39	153.36	1.94	0.2585
EP	K_{low}	140	138.03	133.63	8.80	2.08×10^{-7}
	K_{mid}	150	149.71	143.89	11.64	1.35×10^{-11}
	K_{high}	160	156.55	152.43	8.24	8.88×10^{-7}

Stiffness values are identified at zero velocity ($\dot{x} = 0$) and maximum velocity ($\dot{x} = \dot{x}_{\max}$). Δ denotes the absolute change in stiffness between $\dot{x} = 0$ and $\dot{x} = \dot{x}_{\max}$, normalized by the theoretical stiffness range (126-176 N/mm). p -values are obtained from pairwise statistical comparison between $\dot{x} = 0$ and $\dot{x} = \dot{x}_{\max}$.

The stiffness variation is quantified as

$$\Delta(\%) = \frac{|K_{\dot{x}=0} - K_{\dot{x}=\dot{x}_{\max}}|}{K_{\max, \text{theory}} - K_{\min, \text{theory}}} \times 100\%,$$

where $K_{\min, \text{theory}} = 126$ N/mm and $K_{\max, \text{theory}} = 176$ N/mm define the theoretical stiffness range.

VI. CONCLUSION

This paper presented a hybrid Neural ODE framework for modeling antagonistic pneumatic artificial muscle (PAM) dynamics. By embedding parametric joint mechanics and pressure

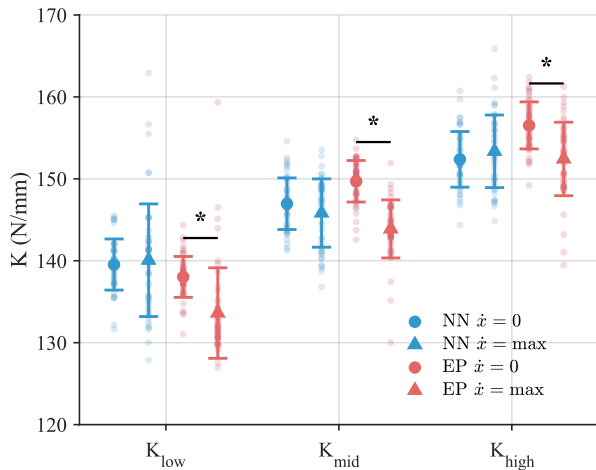


Fig. 9: Experimentally identified stiffness for commands generated by the Neural ODE (NN) and equilibrium point (EP) models at three nominal stiffness levels (K_{low} , K_{mid} , K_{high}). Circles denote perturbations at zero velocity ($\dot{x} = 0$); triangles denote perturbations at maximum velocity ($\dot{x} = \max$). Large markers show mean \pm standard deviation; faded dots show individual measurements. Asterisks indicate statistically significant differences between velocity conditions for the EP model ($p < 0.05$, paired t -test). The NN model maintains consistent stiffness across velocities, while the EP model shows a systematic reduction at maximum velocity.

dynamics into a continuous-time learning formulation, the approach captures coupled motion, pneumatic state evolution, and nonlinear antagonistic force behavior in a physically structured yet data-driven manner.

The learned forward model accurately predicts joint motion and chamber pressures across 225 co-contraction conditions, and the learned force-displacement relationships exhibit equilibrium shifts with mass imbalance, stiffness scaling with co-contraction, and velocity-dependent hysteresis consistent with PAM behavior. A feedforward input synthesis procedure derived from the learned dynamics was validated experimentally, confirming reliable motion and stiffness prediction across varying amplitudes, frequencies, and co-contraction levels. Comparison with an equilibrium-point model demonstrated that velocity-dependent force modeling improves stiffness consistency across operating conditions.

The framework is trained and validated offline within the operating range covered by the training data. Future work will focus on online adaptation, broader excitation regimes, and extension to multi-degree-of-freedom wearable robotic systems.

REFERENCES

- [1] J. Realmuto and T. Sanger, "A robotic forearm orthosis using soft fabric-based helical actuators," in *2019 2nd IEEE International Conference on Soft Robotics (RoboSoft)*. IEEE, 2019, pp. 591–596.
- [2] S. Sridar, P. H. Nguyen, M. Zhu, Q. P. Lam, and P. Polygerinos, "Development of a soft-inflatable exosuit for knee rehabilitation," in *2017 IEEE/RSJ International Conference on Intelligent Robots and Systems (IROS)*. IEEE, 2017, pp. 3722–3727.
- [3] A. T. Asbeck, S. M. De Rossi, K. G. Holt, and C. J. Walsh, "A biologically inspired soft exosuit for walking assistance," *The International Journal of Robotics Research*, vol. 34, no. 6, pp. 744–762, 2015.
- [4] E. Bardi, M. Gandolla, F. Braghin, F. Resta, A. L. Pedrocchi, and E. Ambrosini, "Upper limb soft robotic wearable devices: a systematic review," *Journal of NeuroEngineering and Rehabilitation*, vol. 19, no. 1, p. 87, 2022.
- [5] E. Kelasidi, G. Andrikopoulos, G. Nikolakopoulos, and S. Manesis, "A survey on pneumatic muscle actuators modeling," in *2011 IEEE International Symposium on Industrial Electronics*. IEEE, 2011, pp. 1263–1269.
- [6] A. Pagoli, F. Chapelle, J.-A. Corrales-Ramon, Y. Mezouar, and Y. Lapusta, "Review of soft fluidic actuators: Classification and materials modeling analysis," *Smart Materials and Structures*, vol. 31, no. 1, p. 013001, 2021.
- [7] Y. Zhang, H. Liu, T. Ma, L. Hao, and Z. Li, "A comprehensive dynamic model for pneumatic artificial muscles considering different input frequencies and mechanical loads," *Mechanical Systems and Signal Processing*, vol. 148, p. 107133, 2021.
- [8] M. S. Xavier, C. D. Tawk, A. Fleming, A. Zolfagharian, J. Pinski, D. Howard, T. Young, J. Lai, S. M. Harrison, Y. K. Yong *et al.*, "Soft pneumatic actuators: A review of design, fabrication, modeling, sensing, control and applications," 2022.
- [9] H. Schulte, "The characteristics of the mckibben artificial muscle," *The application of external power in prosthetics and orthotics*, pp. 94–115, 1961.
- [10] C.-P. Chou and B. Hannaford, "Measurement and modeling of mckibben pneumatic artificial muscles," *IEEE Transactions on robotics and automation*, vol. 12, no. 1, pp. 90–102, 1996.
- [11] N. Hogan, "Adaptive control of mechanical impedance by coactivation of antagonist muscles," *IEEE Transactions on Automatic Control*, pp. 681–690, 1984.
- [12] A. G. Feldman, "Once more on the equilibrium-point hypothesis (λ model) for motor control," *Journal of motor behavior*, vol. 18, no. 1, pp. 17–54, 1986.
- [13] Y. Ariga, H. T. Pham, M. Uemura, H. Hirai, and F. Miyazaki, "Novel equilibrium-point control of agonist-antagonist system with pneumatic artificial muscles," in *2012 IEEE International Conference on Robotics and Automation*. IEEE, 2012, pp. 1470–1475.
- [14] A. Tödtheide, T. Lilge, and S. Haddadin, "Antagonistic impedance control for pneumatically actuated robot joints," *IEEE Robotics and Automation Letters*, vol. 1, no. 1, pp. 161–168, 2015.
- [15] N. Hogan, "Impedance control: An approach to manipulation: Part ii—implementation," *Journal of dynamic systems, measurement, and control*, vol. 107, no. 1, pp. 8–16, 1985.
- [16] M. Doumit, A. Fahim, and M. Munro, "Analytical modeling and experimental validation of the braided pneumatic muscle," *IEEE transactions on robotics*, vol. 25, no. 6, pp. 1282–1291, 2009.
- [17] A. Hošovský and M. Havran, "Dynamic modelling of one degree of freedom pneumatic muscle-based actuator for industrial applications," *Tehnički vjesnik*, vol. 19, no. 3, pp. 673–681, 2012.
- [18] T. V. Minh, B. Kamers, H. Ramon, and H. Van Brussel, "Modeling and control of a pneumatic artificial muscle manipulator joint—part i: Modeling of a pneumatic artificial muscle manipulator joint with accounting for creep effect," *Mechatronics*, vol. 22, no. 7, pp. 923–933, 2012.
- [19] A. Hošovský, J. Pitel, and K. Židek, "Enhanced dynamic model of pneumatic muscle actuator with elman neural network," in *Abstract and Applied Analysis*, vol. 2015, no. 1. Wiley Online Library, 2015, p. 906126.
- [20] K. K. Ahn and H. P. H. Anh, "Comparative study of modeling and identification of the pneumatic artificial muscle (pam) manipulator using recurrent neural networks," *Journal of Mechanical Science and Technology*, vol. 22, no. 7, pp. 1287–1298, 2008.
- [21] M. T. Gillespie, C. M. Best, E. C. Townsend, D. Wingate, and M. D. Killpack, "Learning nonlinear dynamic models of soft robots for model predictive control with neural networks," in *2018 IEEE International Conference on Soft Robotics (RoboSoft)*. IEEE, 2018, pp. 39–45.
- [22] P. Hyatt, D. Wingate, and M. D. Killpack, "Model-based control of soft actuators using learned non-linear discrete-time models," *Frontiers in Robotics and AI*, vol. 6, p. 22, 2019.
- [23] W. Sun, N. Akashi, Y. Kuniyoshi, and K. Nakajima, "Physics-informed recurrent neural networks for soft pneumatic actuators," *IEEE Robotics and Automation Letters*, vol. 7, no. 3, pp. 6862–6869, 2022.
- [24] G. Wang, R. Chalard, J. Cifuentes, and M. T. Pham, "Learning an inverse thermodynamic model for pneumatic artificial muscles control," *Mechatronics*, vol. 110, p. 103359, 2025.

- [25] S. Wang, R. Wang, Y. Liu, Y. Zhang, and L. Hao, "Dynamic modeling and control of pneumatic artificial muscles via deep lagrangian networks and reinforcement learning," *Engineering Applications of Artificial Intelligence*, vol. 148, p. 110406, 2025.
- [26] J. Magdy, O. M. Shehata, H. A. Kandil, and E. I. Morgan, "Hybrid modelling, control and simulation of knee joint actuated by antagonistic pneumatic artificial muscles," *International Journal of Mechanical Engineering and Robotics Research*, vol. 14, no. 4, 2025.
- [27] K. Zhou, Q. Zong, B. Zhang, D. Liu, T. Liu, Q. Zhu, and B. Wang, "Model predictive control of pneumatic artificial muscle antagonist joint angle tracking based on bp neural network modelling," *IEEE Sensors Journal*, 2025.
- [28] W. Zhao and A. Song, "Active motion control of a knee exoskeleton driven by antagonistic pneumatic muscle actuators," in *Actuators*, vol. 9, no. 4. MDPI, 2020, p. 134.
- [29] M. Trumić, K. Jovanović, and A. Fagiolini, "Decoupled nonlinear adaptive control of position and stiffness for pneumatic soft robots," *The International Journal of Robotics Research*, vol. 40, no. 1, pp. 277–295, 2021.
- [30] T. Shin, T. Ibayashi, and K. Kogiso, "Detailed dynamic model of antagonistic pam system and its experimental validation: Sensorless angle and torque control with ukf," *IEEE/ASME Transactions on Mechatronics*, vol. 27, no. 3, pp. 1715–1726, 2021.
- [31] T. Shin and K. Kogiso, "Sensorless angle and stiffness control of antagonistic pam actuator using reference set," *Advanced Robotics*, vol. 36, no. 9, pp. 423–437, 2022.
- [32] R. T. Chen, Y. Rubanova, J. Bettencourt, and D. K. Duvenaud, "Neural ordinary differential equations," *Advances in neural information processing systems*, vol. 31, 2018.